Computational Method for Evaluating the Thermoelectric Power Factor for Organic Materials Modeled by the Holstein Model: A Time-Dependent Density Matrix Renormalization Group Formalism

Yufei Ge, Weitang Li, Jiajun Ren, and Zhigang Shuai*

Read Online

ACCESS | Metrics & More | Article Recommendations | Supporting Information

ABSTRACT: Organic/polymeric materials are of emerging importance for thermoelectric conversion. The soft nature of these materials implies strong electron−phonon coupling, often leading to carrier localization. This poses great challenges for the conventional Boltzmann transport description based on relaxation time approximation and band structure calculations. In this work, combining the Kubo formula with the finite-temperature time-dependent density matrix renormalization group (FT-TD-DMRG) in the grand canonical ensemble, we developed a nearly exact algorithm to calculate the thermoelectric power factor $PF = \alpha^2 \sigma$, where α is the Seebeck coefficient and σ is the electrical conductivity, and apply the algorithm to Holstein Hamiltonian with electron−phonon coupling to model organic materials. Our algorithm can provide a unified description covering the weak coupling limit described by the bandlike Boltzmann transport to the strong coupling hopping limit.

Thermoelectric Power Factor $PF = \alpha^2 \sigma$
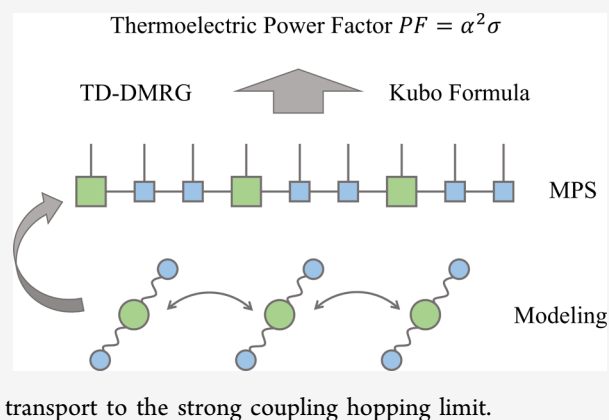
1. INTRODUCTION

Organic/polymeric materials are potential candidates for next-generation high-performance thermoelectric materials because of their remarkable low thermal conductivity, relatively high electrical conductivity by doping, structural flexibility, lightweight, low toxicity, and biocompatibility.[1−6] Past decades have witnessed rapid development in the field, and a number of promising organic/polymeric thermoelectric materials have been synthesized, varying from small molecular systems[1,7] to conducting polymers.[8,9] However, the thermoelectric figure of merit ZT for organic materials is still low compared to the inorganic counterpart, mainly because of the low power factor PF. Here, $ZT = \frac{\alpha^2 \sigma T}{\kappa}$, which measures the thermoelectric conversion efficiency and power factor is defined as $PF = \alpha^2 \sigma$. σ, α, and κ are the electrical conductivity, Seebeck coefficient that measures the voltage drop divided by the temperature difference, and thermal conductivity, respectively, at temperature T.[10]

First-principle band structure calculations have been extensively applied to investigate thermoelectric conversion. It assumes that both electron correlation and electron−phonon coupling are weak and thus the electrons are delocalized. Therefore, the charge transport process is wavelike with scatterings by phonons, impurities, disorders, etc..[11,12] Combining the band structure with the Boltzmann transport equation and Matthiessen's rule, the thermoelectric transport property has been calculated for a number of systems.[13−16]

Meanwhile, it should be borne in mind that the most important characteristic of organic/polymeric materials lies in the structural flexibility and the disorders/impurities.[17−21] On the other hand, from the perspective of device physics modeling, the hopping model has been widely employed to describe carrier transport in organic optoelectronics. The origin of carrier localization relies on the assumption of strong electron−phonon coupling, and thus carriers travel through the system via a hopping process.[22−24] With the assistance of numerical simulation, plenty of studies have been carried out on the hopping limit.[24−26]

However, the strength of electron−phonon coupling and the charge transfer integral are comparable in most organic materials. This indicates a polaron transport that is neither bandlike nor hopping.[27,28] In fact, polaron describes such charge carriers moving along with the surrounding lattice distortion.[29,30] Efforts have been devoted to going beyond the simple descriptions of hopping or band. Different time scales for intermolecular vibrations, intramolecular vibrations, and intermolecular charge transfer have been taken into account.[30−32] Since the intramolecular vibration is much faster
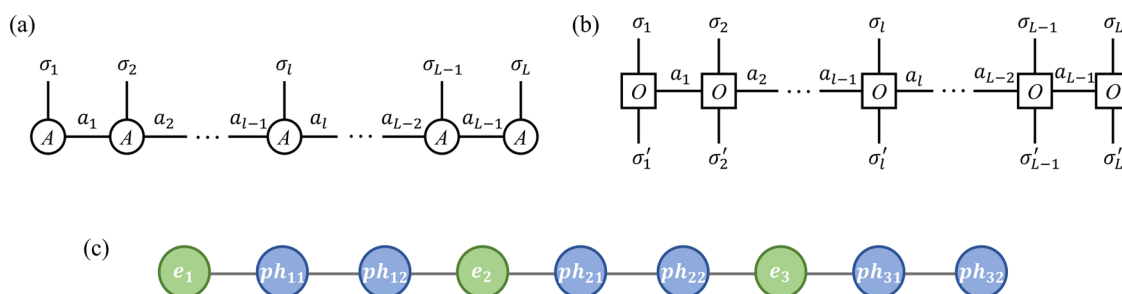
(a)

(b)

(c)
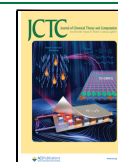
Figure 1. Schematic diagram of (a) MPS and (b) MPO. (c) Mapping a three-site system with two vibration modes per site into a one-dimensional chain structure.

than intermolecular charge transfer, the intramolecular electron–phonon coupling has been treated as a mean-field via polaron transformation,[33−35] through which, the dependence of the Seebeck coefficient on the doping level (chemical potential), electron–phonon coupling strength, and temperature has been unraveled.[36−38] On the other hand, intermolecular vibration is much slower than intermolecular charge transfer. Thus, it can often be approximated classical mechanically through mixed quantum-classical approaches.[32,39−41] Combining numerical calculation and theoretical analysis, transient localization theory has been developed for organic materials' charge transport,[42−45] emphasizing the vital role of intermolecular electron–phonon coupling in the charge transport of organic materials. Although these approaches provide insightful results in the regimes where the underlying assumption is valid, their accuracy remains unclear in the broad parameter regimes, especially the intermediate coupling regime, which is believed to be relevant to high-performance organic materials. A general method for thermoelectric transport in organic materials is still absent. The main difficulty lies in the unavoidable many-body problem arising from the comparable charge transfer integral and inter/intramolecular electron–phonon coupling, which limits the range of application of analytic approaches and the accuracy of numerical methods.

The density matrix renormalization group (DMRG) is a numerically accurate and robust method for many-body problems.[46] Since the establishment by White in 1992,[47] numerous algorithms have been developed, including time-evolution algorithms,[48,49] finite-temperature algorithms,[50] etc. The rapid development of algorithms enables DMRG to tackle various problems, including strong correlation lattice models,[51] ab initio electronic structure,[52,53] and excited-state dynamics.[54] The recent development of GPU acceleration algorithms[55] and matrix product operator (MPO) autoconstruction algorithms[56] further broadens the application scope of DMRG in simulating the dynamics of complex systems. Very recently, Li et al. presented a general picture of the mobility of organic semiconductors by combining time-dependent DMRG (TD-DMRG) with the Kubo formula,[57,58] indicating that TD-DMRG is a possible solution for organic thermoelectric transport in broad parameter space.

In this work, we develop an algorithm based on the finite-temperature time-dependent density matrix renormalization group (FT-TD-DMRG) in the grand canonical ensemble to calculate the power factor of organic materials described by the Holstein model. We demonstrate that FT-TD-DMRG is a powerful method for investigating the organic thermoelectric transport process, which can bridge the gap between the hopping picture and band picture. A detailed theoretical framework and numerical outcomes are provided in the following sections.

2. MODEL AND ALGORITHM

2.1. Introduction of Model. The Holstein model is widely used to capture the effect of electron–phonon coupling in
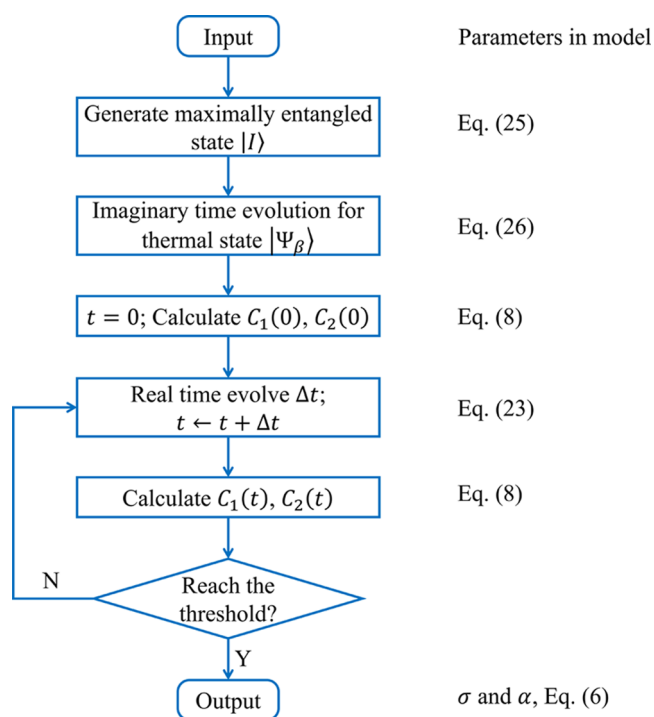

Figure 2. Summary of the TD-DMRG method for the thermoelectric power factor.

organic materials. We consider a one-dimensional molecular chain in this work and the Hamiltonian is[59]

$$\hat{H} = \hat{H}_{e} + \hat{H}_{e-ph} + \hat{H}_{ph} \tag{1}$$

where the electronic part is

$$\hat{H}_{e} = \sum_{j} \epsilon_{j}\hat{a}_{j}^{\dagger}\hat{a}_{j} + \sum_{j} \tau_{j}(\hat{a}_{j}^{\dagger}\hat{a}_{j+1} + \hat{a}_{j+1}^{\dagger}\hat{a}_{j}) \tag{2}$$

and the phonon part is

$$\hat{H}_{ph} = \sum_{j,n} \hbar\omega_{n}\left(\hat{b}_{jn}^{\dagger}\hat{b}_{jn} + \frac{1}{2}\right) \tag{3}$$

and the electron−phonon coupling term is

$$\hat{H}_{e-ph} = \sum_{j,n} \hbar g_n \omega_n (\hat{b}_{jn}^\dagger + \hat{b}_{jn}) \hat{a}_j^\dagger \hat{a}_j \tag{4}$$

Here, $\hat{a}_j^\dagger$ and $\hat{a}_j$ are creation and annihilation operators of an electron at site j. $\hat{b}_{jn}^\dagger$ and $\hat{b}_{jn}$ are creation and annihilation operators of the nth intramolecular vibration mode at site j with the coupling constant g_n and vibration frequency ω_n. ϵ_j and τ_j are the site energy at site j and the charge transfer integral between site j and $j + 1$. The reorganization energy $\lambda = \sum_n g_n^2 \omega_n$ characterizes the strength of electron−phonon coupling.

As far as carrier transport is concerned, there exist two extreme cases, the bandlike limit and hopping limit. "Bandlike" describes carriers at well delocalized and fully coherent electronic states, like in a pure inorganic crystal where the transport behavior is governed by weak electron−phonon scattering, often described by the Boltzmann transport equation under the relaxation time approximation, while the "hopping" mechanism describes the localized charge transport where the localization could be originated from disorders, impurities, or strong electron−phonon coupling. In the Holstein model, for $\tau_j \ll \lambda$, the strong electron−phonon coupling can lead to electron localization and the model reduces to a typical hopping model. When $\tau_j \gg \lambda$, electrons are delocalized and slightly influenced by small electron−phonon coupling, leading to a typical band model.

The thermoelectric power factor PF is defined as

$$PF = \alpha^2 \sigma \tag{5}$$

Conductivity σ and Seebeck coefficient (thermopower) α can be calculated via the Kubo formula[36,60]

$$\begin{cases} \sigma = \dfrac{1}{k_B T} L_{11} \\ \alpha = \dfrac{1}{T} \dfrac{L_{12}}{L_{11}} \end{cases} \tag{6}$$

Here, k_B is the Boltzmann constant and T is the temperature. L_{11} and L_{12} are defined as

$$\begin{cases} L_{11} = \dfrac{1}{2V} \displaystyle\int_{-\infty}^{+\infty} C_1(t)\, dt \\ \qquad = \dfrac{1}{V} \displaystyle\int_0^{+\infty} \mathrm{Re}\, C_1(t)\, dt \\ L_{12} = \dfrac{1}{2V} \displaystyle\int_{-\infty}^{+\infty} C_2(t)\, dt \\ \qquad = \dfrac{1}{V} \displaystyle\int_0^{+\infty} \mathrm{Re}\, C_2(t)\, dt \end{cases} \tag{7}$$

with correlation functions

$$\begin{cases} C_1(t) = \mathrm{Tr}[\hat{\rho}_0 e^{i\hat{H}t/\hbar} \hat{J}_e e^{-i\hat{H}t/\hbar} \hat{J}_e] \\ C_2(t) = \mathrm{Tr}[\hat{\rho}_0 e^{i\hat{H}t/\hbar} \hat{J}_Q e^{-i\hat{H}t/\hbar} \hat{J}_e] \end{cases} \tag{8}$$

where $\hat{J}_e$ and $\hat{J}_Q$ are the electric current and heat current operators, respectively, and V is the volume: $V = NA\Omega$, where N is the total site number, A is the cross-sectional area, and Ω is the lattice spacing. Meanwhile, the thermoelectric transport process involves both the electron current and heat current,

containing both particle exchange and energy exchange. Therefore, it is necessary to adopt the grand canonical ensemble to describe such a process, by which, the density operator is

$$\hat{\rho}_0 = \frac{1}{Z} e^{-\beta(\hat{H} - \mu \hat{N}_e)} \tag{9}$$

where $Z = \mathrm{Tr}[e^{-\beta(\hat{H} - \mu \hat{N}e)}]$ is the partition function and μ is the chemical potential, $\beta = (k_B T)^{-1}$, and the electron number operator $\hat{N}_e = \sum_j \hat{a}_j^\dagger \hat{a}_j$. In the grand canonical ensemble, the mean number of electrons in the system $n_e = \mathrm{Tr}[\hat{N}_e \hat{\rho}_0]$ depends on μ. We can adjust μ via the bisection method to reach the target n_e, considering n_e increases monotonically with μ. Here, we define the doping ratio $c = n_e/N$ as the number of electrons in the system divided by the maximum number of electrons that the system can hold. Obviously, c is related to the carrier concentration of the system.

The electric current operator $\hat{J}_e$ and heat current operator $\hat{J}_Q$ are derived through a commutator with Holstein Hamiltonian (see Supporting Information 1)

$$\hat{J}_e = -\frac{i}{\hbar} e\Omega \sum_j \tau_j (\hat{a}_{j+1}^\dagger \hat{a}_j - \hat{a}_j^\dagger \hat{a}_{j+1}) \tag{10}$$

$$\hat{J}_Q = \hat{J}_Q^I + \hat{J}_Q^{II} \tag{11}$$

$$\hat{J}_Q^I = -\frac{i}{\hbar} \Omega \sum_j \tau_j \tau_{j+1} (\hat{a}_{j+2}^\dagger \hat{a}_j - \hat{a}_j^\dagger \hat{a}_{j+2}) \tag{12}$$

$$\hat{J}_Q^{II} = -\frac{i}{\hbar} \Omega \sum_j \left[\frac{1}{2}(\hat{E}_j + \hat{E}_{j+1}) - \mu \right] \tau_j (\hat{a}_{j+1}^\dagger \hat{a}_j - \hat{a}_j^\dagger \hat{a}_{j+1}) \tag{13}$$

Here, we define

$$\hat{E}_j = \epsilon_j + \sum_n \hbar g_n \omega_n (\hat{b}_{jn}^\dagger + \hat{b}_{jn}) \tag{14}$$

2.2. TD-DMRG Algorithm and Realization.
2.2.1. MPS and MPO. The second generation of DMRG adopts a matrix product state (MPS) ansatz with a finite truncation of the virtual bond dimension to approximate the exact wave function $|\Psi\rangle$ efficiently[48]

$$|\Psi\rangle \cong \sum_{\{a_l\},\{\sigma_l\}} A_{a_1}^{\sigma_1} A_{a_1,a_2}^{\sigma_2} \dots A_{a_{L-1}}^{\sigma_L} |\sigma_1 \sigma_2 \dots \sigma_L\rangle \tag{15}$$

Here, σ_l is the physical index at site l, ranging from 1 to d_l. For electron or spin sites, $d_l = 2$, representing the occupied and unoccupied states or spin-down and spin-up states. For phonon sites, $d_l = d_H$, where d_H is the size of the local phonon basis. Theoretically, d_H should be infinitely large while a reasonably finite d_H can provide rather accurate outcomes in most cases. a_l is the index of the virtual bond between site l and site $l + 1$, ranging from 1 to D_l. With a careful selection of the upper bound D of D_l, the exact wave function $|\Psi\rangle$ can be approximated efficiently with high accuracy. The graphic illustration of MPS is presented in Figure 1a.

Similarly, the operator $\hat{O}$ can be expressed as a matrix product operator (MPO) form exactly, as presented in Figure 1b.

$$\hat{O} = \sum_{\{a_l\},\{\sigma_l\},\{\sigma_l'\}} O_{a_1}^{\sigma_1,\sigma_1'} O_{a_1,a_2}^{\sigma_2,\sigma_2'} ... O_{a_{L-1}}^{\sigma_L,\sigma_L'} |\sigma_1\sigma_2...\sigma_L\rangle\langle\sigma_1'\sigma_2'...\sigma_L'|$$

(16)

There exist a number of schemes to construct the MPO of a generic operator, and in this work, we adopted the graph-based automated construction algorithm developed by Ren et al.[56] to obtain the most compact MPO with the minimum bond dimension. After defining MPS and MPO, the calculation of quantities such as the expectation value simply becomes tensor contraction. We map the degrees of freedom (DoFs) of the electrons and phonons into a chain structure where the DoFs of one molecule are arranged together and phonons with a lower frequency are closer to electron sites, as presented in Figure 1c. Such sorting can lead to a fast convergence with the bond dimension (Supporting Information 3).[61−64]

2.2.2. Time-Evolution Algorithm.

Time evolution is involved in calculating the correlation functions in eq 8. Various time evolution methods have been developed,[48,49,65,66] including direct evolution and compression, time step-targeting, time-dependent variational principle, and so on. In this work, we adopt the time-dependent variational principle with a projector-splitting algorithm (TDVP-PS) for time evolution, which has been proved efficient and robust, especially with the hybrid CPU−GPU heterogeneous algorithms.[49,55] The basic idea of TDVP-PS is to project $\hat{H}|\Psi\rangle$ onto the tangent space of the current MPS via the projection operator[67] $\hat{P}$

$$\frac{\partial|\Psi(t)\rangle}{\partial t} = -i\hat{P}\hat{H}|\Psi(t)\rangle$$

(17)

$$\hat{P} = \sum_{l=1}^{L} \hat{P}[1:l-1] \otimes \hat{I}_l \otimes \hat{P}[l+1:L] - \sum_{l=1}^{L-1} \hat{P}[1:l] \otimes \hat{P}[l+1:L]$$

(18)

Here,

$$\hat{P}[1:l] = \sum_{\substack{\sigma_1,...,\sigma_l;a_1,...,a_l \\ \sigma_1',...,\sigma_l';a_1,...,a_{l-1}}} A_{a_1}^{\sigma_1}...A_{a_{l-1},a_l}^{\sigma_l} A_{a_1'}^{*\sigma_1'}...A_{a_{l-1}',a_l}^{*\sigma_l'} |\sigma_1...\sigma_l\rangle\langle\sigma_1'...\sigma_l'|$$

(19)

$$\hat{P}[l:L] = \sum_{\substack{\sigma_l,...,\sigma_L;a_{l-1},...,a_{L-1} \\ \sigma_l',...,\sigma_L';a_l,...,a_{L-1}}} B_{a_{l-1},a_l}^{\sigma_l}...B_{a_{L-1}}^{\sigma_L} B_{a_{l-1}',a_l}^{*\sigma_l'}...B_{a_{L-1}'}^{*\sigma_L'} |\sigma_l...\sigma_L\rangle\langle\sigma_l'...\sigma_L'|$$

(20)

$$\hat{I}_l = \sum_{\sigma_l} |\sigma_l\rangle\langle\sigma_l|$$

(21)

$$\hat{P}[1:0] = \hat{P}[L+1:L] = 1$$

(22)

Here, tensors A and B are expressed in left-canonical and right-canonical forms, respectively.

For a tiny time step Δt, eq 17 can be solved as

$$|\Psi(t+\Delta t)\rangle = e^{-i\hat{P}\hat{H}\Delta t/\hbar}|\Psi(t)\rangle$$

(23)

The propagator is split into multiple subterms through a second-order Trotter decomposition, each of which is applied successively in a sweep process. The time evolution step Δt should be carefully chosen to balance accuracy and efficiency.

2.2.3. Finite-Temperature Algorithm for Grand Canonical Ensemble.

Temperature is introduced through a purification procedure for the thermal state. The latter is spanned in a direct product space of the physical space P and an auxiliary space Q chosen as an exact copy of P. Then, the thermal ensemble average $\langle O \rangle$ at T can be expressed as the expectation value of the pure thermal state $|\Psi_\beta\rangle$ (we suppose $|\Psi_\beta\rangle$ is normalized and $\beta = (k_B T)^{-1}$)

$$\langle O \rangle = \text{Tr}[\hat{O}\hat{\rho}] = \langle\Psi_\beta|\hat{O}|\Psi_\beta\rangle$$

(24)

By defining the maximally entangled state $|I\rangle$

$$|I\rangle = \prod_l \sum_{\sigma_l} \frac{1}{\sqrt{d_l}} |\sigma_l\rangle_P |\sigma_l\rangle_Q$$

(25)

The maximally entangled state means that all states are occupied with equal possibilities. In a maximally entangled state, the entanglement between the DoFs of site l in physical space P and auxiliary space Q is maximal, while no entanglement exists between different DoFs. Therefore, the maximally entangled state $|I\rangle$ can be expressed efficiently as presented in refs 46, 48. The thermal state can be obtained via imaginary time evolution on the maximally entangled state $|I\rangle$ from $t = 0$ to $t = -i\beta/2$[48,68]

$$|\Psi_\beta\rangle = e^{-\beta(\hat{H}-\mu\hat{N}_e)/2}|I\rangle$$

(26)

Lower T (larger β) needs a larger number of imaginary time evolution steps N_{imag}. Note that in imaginary time evolution, the number of electrons n_e can change since the grand canonical ensemble is adopted.

2.2.4. Jordan−Wigner Transformation for a Many-Electron System.

In previous investigations for carrier mobility, the density is low so that one considered only one charge in the system. However, for thermoelectric conversion, doping is important to achieve optimal thermopower. So, here comes the issue of anticommutation for multifermions. When constructing an MPO, to fulfill the antisymmetric property of electrons, the Jordan−Wigner transformation is adopted[69] to transform the electron basis to the spin basis

$$\begin{cases} \hat{a}_j^\dagger = \prod_{k=1}^{j-1}(-\hat{\sigma}_k^z)\cdot\hat{\sigma}_j^+ \\ \hat{a}_j = \prod_{k=1}^{j-1}(-\hat{\sigma}_k^z)\cdot\hat{\sigma}_j^- \end{cases}$$

(27)

Here, $\hat{\sigma}^z$, $\hat{\sigma}^+$, and $\hat{\sigma}^-$ are Pauli operators of the spin basis, which commute between different sites

$$[\hat{\sigma}_l^{z,+,-}, \hat{\sigma}_m^{z,+,-}] = 0, \ (l \neq m)$$

(28)

2.2.5. Algorithm Flow Chart.

In summary, we can reformulate the correlation functions in eq 8 as follows and calculate α and σ via the procedure presented in Figure 2
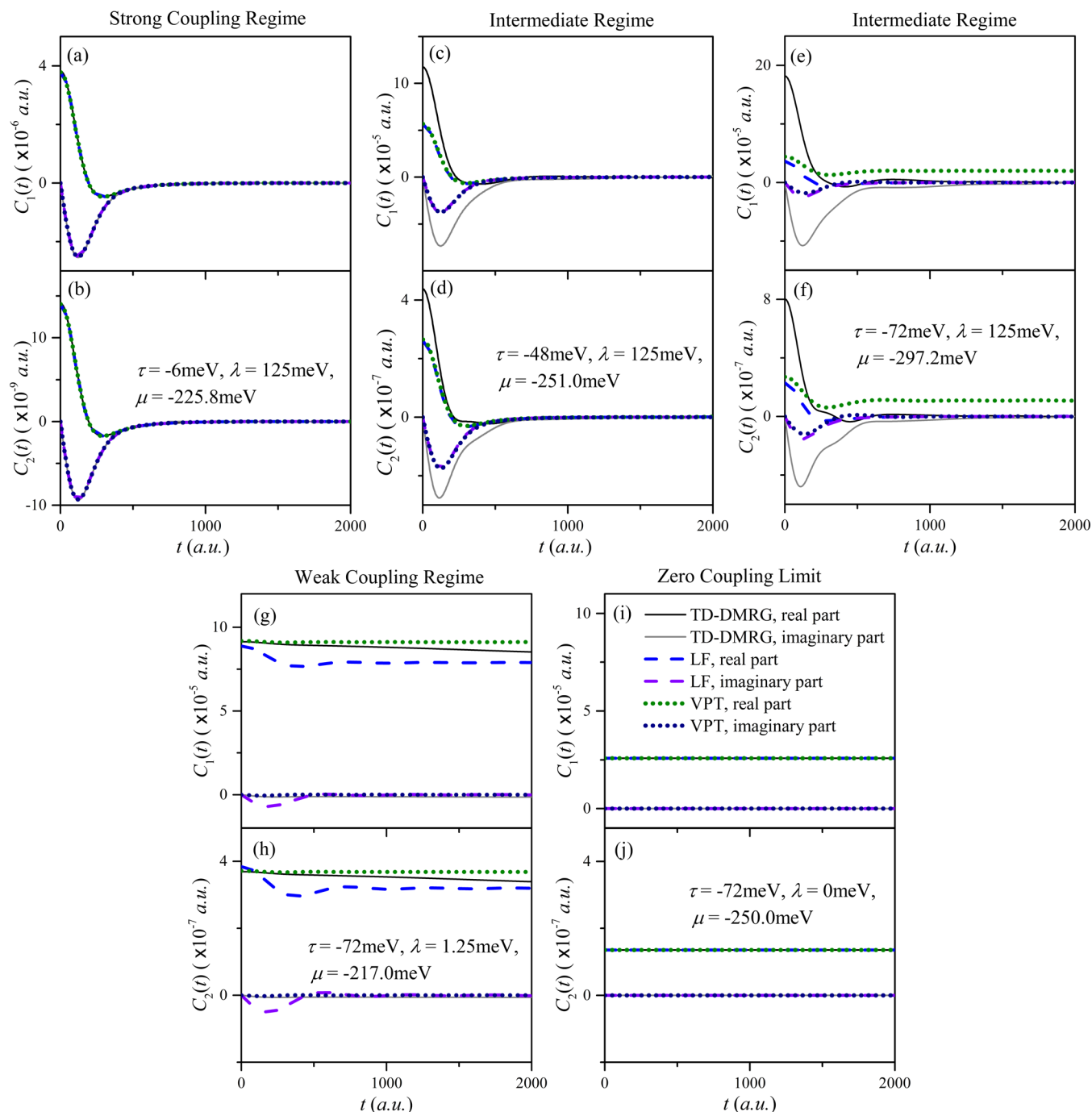
Figure 3. Comparison of the real and imaginary parts of correlation functions $C_1(t)$ and $C_2(t)$ calculated by the time-dependent density matrix renormalization group (TD-DMRG), Lang−Firsov polaron transformation (LF), and variational polaron transformation (VPT) in different regimes; (a, b) are in the strong coupling regime where $\tau \ll \lambda$; (c), (d), (e), and (f) are in the intermediate regime where τ and λ are comparable; (g, h) are in the weak coupling regime where $\tau \gg \lambda$; (i, j) are in the zero coupling limit where $\lambda = 0$ indicates that $g_n = 0$ and no electron−phonon coupling exists. Here, we set $T = 300\ K$, $N = 20$, $D = 48$, $d_H = 12$, $N_{imag} = 300$, and $\Delta t = 10.0$ au.

$$
\begin{cases}
C_1(t) = \mathrm{Tr}[\hat{\rho}_0 e^{i\hat{H}t/\hbar}\hat{J}_e e^{-i\hat{H}t/\hbar}\hat{J}_e] \\
\qquad = \langle \Psi_\beta | e^{i\hat{H}t/\hbar}\hat{J}_e e^{-i\hat{H}t/\hbar}\hat{J}_e |\Psi_\beta \rangle \\
C_2(t) = \mathrm{Tr}[\hat{\rho}_0 e^{i\hat{H}t/\hbar}\hat{J}_Q e^{-i\hat{H}t/\hbar}\hat{J}_e] \\
\qquad = \langle \Psi_\beta | e^{i\hat{H}t/\hbar}\hat{J}_Q e^{-i\hat{H}t/\hbar}\hat{J}_e |\Psi_\beta \rangle
\end{cases}
\tag{29}
$$

As shown in Figure 2, we input a set of parameters (note that the computational parameters presented in section 3.1

should be checked) and the maximally entangled state $|I\rangle$ ($\beta = 0$) is taken as the initial state. The thermal state $|\Psi_\beta\rangle$ is obtained via several hundred steps of imaginary time evolution from $|I\rangle$. After obtaining $|\Psi_\beta\rangle$, we calculate $\hat{J}_e|\Psi_\beta\rangle$ by applying MPO $\hat{J}_e$ to $|\Psi_\beta\rangle$. In real-time evolution, through continuous application of $e^{i\hat{H}\Delta t/\hbar}$ to bra $\langle\Psi_\beta|$ and $e^{-i\hat{H}\Delta t/\hbar}$ to ket $\hat{J}_e|\Psi_\beta\rangle$, $\langle\Psi_\beta| e^{i\hat{H}t/\hbar}$ and $e^{-i\hat{H}t/\hbar}\hat{J}_e |\Psi_\beta\rangle$ can be calculated. Correlation functions $C_1(t)$ and $C_2(t)$ are calculated by contracting $\langle\Psi_\beta| e^{i\hat{H}t/\hbar}$ and $e^{-i\hat{H}t/\hbar}\hat{J}_e |\Psi_\beta\rangle$ with MPO $\hat{J}_e$ and MPO $\hat{J}_Q$ separately in real-time evolution. The real-time evolution
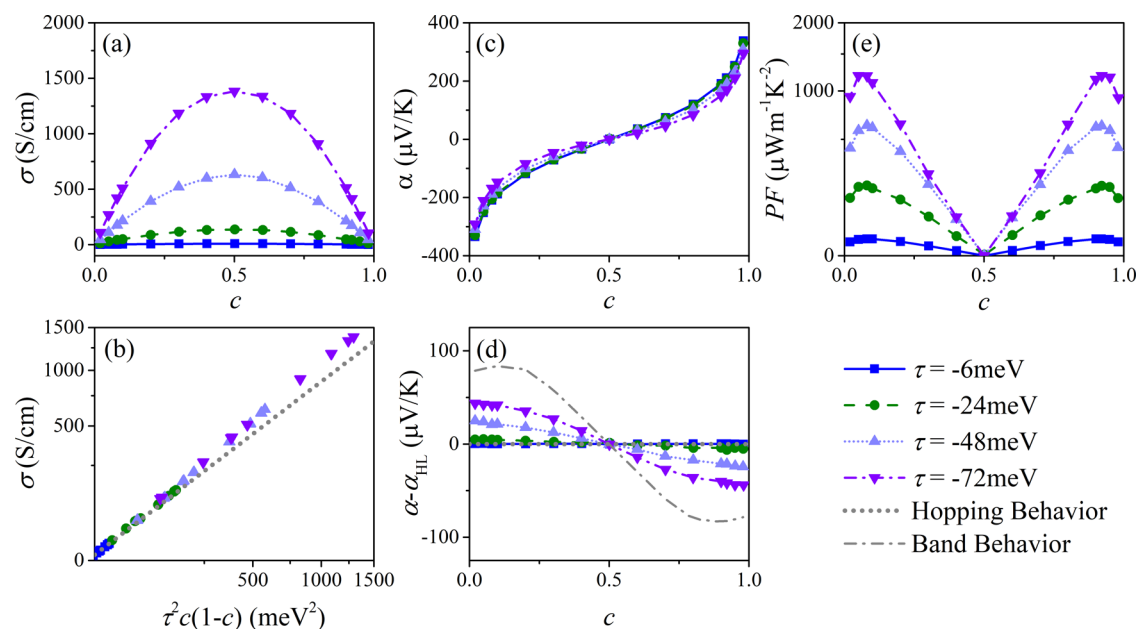
Figure 4. (a, b) are the doping ratio dependence of conductivity σ, (c, d) are the doping ratio dependence of the Seebeck coefficient α, and (e) is the doping ratio dependence of the power factor PF. The hopping behavior in panels (b) and (d) is obtained by the outcome of Fermi's golden rule presented in Supporting Information 5 and $\alpha_{HL} = -\frac{k_B}{e}\ln\frac{c}{1-c}$. The band behavior in panel (d) is calculated with $\tau = -240$ meV and $\lambda = 0$ by the Boltzmann transport theory presented in Supporting Information 4.

continues until correlation functions become less than a threshold set to be $\max\{C_i(t-9\Delta t), C_i(t-8\Delta t),..., C_i(t)\} \leq 5 \times 10^{-3} C_i(0)$, and then the electrical conductivity σ and the Seebeck coefficient α can be obtained by integrating correlation functions as eqs 6 and 7.

3. RESULTS AND DISCUSSION

In this work, we focus on a one-dimensional Holstein model with periodic boundary conditions and assume $\tau_j = \tau$ and $\epsilon_j = \epsilon$ for all sites. Following the work of Wang[37] and Zhao,[36] we choose the carrier reorganization energy $\lambda = 125$ meV (for typical organic semiconductor) and use five intramolecular vibration modes, where $\{\omega_n\} = \{35.6, 106.8, 178.0, 249.2, 320.4 \text{ meV}\}$ and $\{g_n\} = \{1.21, 0.62, 0.35, 0.18, 0.09\}$. The values are taken from the super-Ohmic spectral density function from ref 36, following a discretization scheme (Supporting Information 2). For simplicity, we set the site energy $\epsilon = 0$, cross area $A = 100$ au, and lattice constant $\Omega = 10$ au in all of the calculations.

3.1. Validity of TD-DMRG Algorithm. As mentioned above, the number of imaginary time evolution steps N_{imag}, the size of the bond dimension D, the size of the local phonon basis d_H, the size of the real time evolution step Δt, and the number of sites N are essential parameters to assure the accuracy of calculations. In this work, we focus on the challenging intermediate parameter regime where τ is comparable to λ and the room temperature. In addition, the adoption of the grand canonical ensemble breaks the particle number symmetry, which increases the computational cost. In Supporting Information 3, we demonstrate that in this case, the converged and valid results can be obtained by TD-DMRG with a moderate computational cost. For most of the parameter regimes we are interested in, the parameter set of $\Delta t = 50$, $N = 12$, $D = 48$, and $d_H = 9$ is enough for numerical convergence.

3.2. Comparison with Polaron Transformation. We now compare the correlation functions calculated by TD-DMRG with those obtained from Lang−Firsov polaron transformation[37] (LF) and variational polaron transformation[36] (VPT) (Supporting Information 5) ranging from the strong coupling regime, Figure 3a,b, intermediate coupling regime, Figure 3c−f, and weak coupling regime, Figure 3g,h, to the zero coupling limit, Figure 3i,j.

It is known that the LF/VPT theory is valid in the strong coupling regime. These polaron transformation methods can reproduce the hopping behavior as described by Fermi's golden rule for $\tau \ll \lambda$. These can also reproduce the bandlike behavior as described by the Boltzmann transport equation when λ is negligible, as demonstrated previously[35,36] (see Supporting Information 5). As shown in Figure 3a,b,i, and j, the correlation functions calculated by TD-DMRG coincide closely with LF and VPT in both the strong coupling regime and zero coupling limit, which validates our implementation of TD-DMRG in one sense. Meanwhile, the correlation functions calculated by TD-DMRG are quite different from LF and VPT in the intermediate regime plotted in Figure 3c−f, and larger τ leads to a more obvious difference. Recalling eq 6, the large difference in correlation functions will lead to a large difference in transport coefficients. Note that in LF and VPT, the correlation functions fail to coincide when $t = 0$ in the intermediate coupling regime. Here, LF/VPT's mean-field approximation adopted in eliminating electron−phonon coupling fails, suggesting the weakness of LF and VPT in the intermediate coupling regime. In the weak coupling regime plotted in Figure 3g,h, the difference in correlation functions calculated via different methods starts to disappear, and VPT performs better than LF. These differences imply the limitation of LF/VPT in the intermediate coupling region and the necessity of more accurate numerical methods such as TD-DMRG.
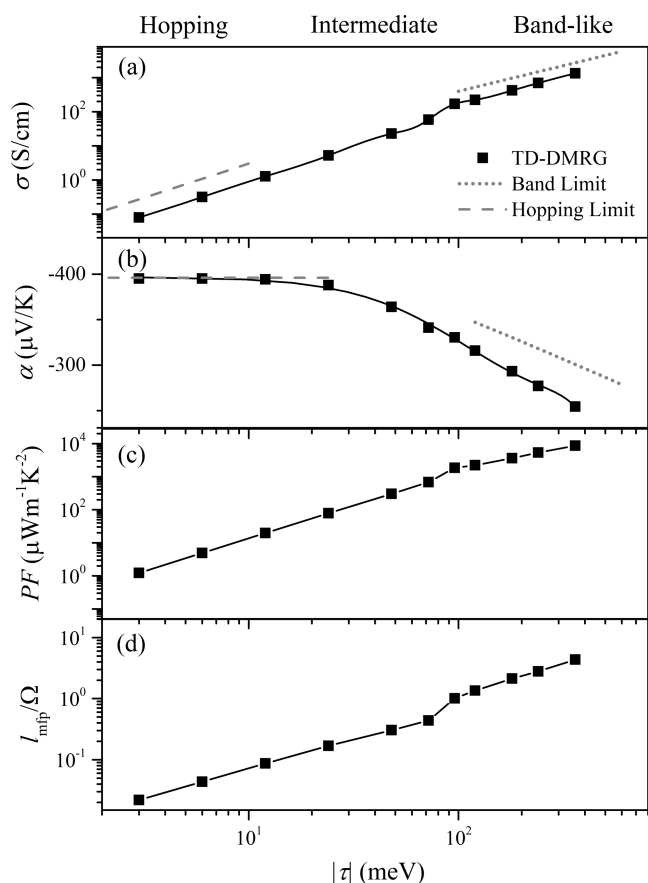
Figure 5. (a) Conductivity σ and (b) Seebeck coefficient α dependence on the transfer integral τ calculated by TD-DMRG (black), hopping limit (gray dashed line), and band limit (gray short dotted line). (c) Power factor PF dependence on τ calculated via TD-DMRG. (d) Mean free path l_{mfp} dependence on τ calculated via TD-DMRG. Here, we set $T = 300$ K and $c = 0.01$.

3.3. Dependence of the Doping Ratio. The dependence of transport coefficients on the doping ratio c is plotted in Figure 4. As shown in Figure 4a, the conductivity increases with increasing c first and then decreases. The maximum value of conductivity is reached when $c = 0.5$, corresponding to the half-filling case where most charge carriers are involved in charge transport. In the hopping limit, the conductivity satisfies[22,29,36] $\sigma \propto \tau^2 c(1 - c)$ when $\tau \ll \lambda$ (Supporting Information 5 and 6), which is plotted in Figure 4b. The $\sigma \propto \tau^2 c(1 - c)$ is satisfied impressively when $\tau = -6$ meV (note that the blue dots sit on the gray short dotted line), and begins to fail as the transfer integral increases (note that the purple dots fall off the gray short dotted line), which is attributed to the transition to the bandlike transport behavior in Section 3.4. The dependence of α on c is also plotted in Figure 4c. The Seebeck coefficient α increases with c and changes sign when $c = 0.5$, corresponding to the change of main carriers from electrons to holes. With a fixed c, the absolute value of α decreases slightly with increasing τ. As reflected in Figure 4d, $\alpha = -\frac{k_B}{e}\ln\frac{c}{1-c}$ holds in the hopping limit[70−72] where $\tau \ll \lambda$ (Supporting Information 6), while the dependence $\alpha = -\frac{k_B}{e}\ln\frac{c}{1-c}$ no longer holds when τ increases (note that $\alpha - \alpha_{\text{HL}}$ is nonzero in Figure 4d). The behavior of $(\alpha - \alpha_{\text{HL}})$ in the band theory (Supporting Information 4) with $\tau = -240$ meV is also plotted for comparison. The similarity of the case τ

$= -72$ meV and the band behavior indicate the transition from the hopping behavior to the band behavior. The power factor PF is also plotted in Figure 4e. Considering the fact that in the hopping limit

$$PF = \alpha^2 \sigma \propto \tau^2 c(1 - c)\left(\ln\frac{c}{1 - c}\right)^2 \tag{30}$$

The maximum of PF is reached when $c = 0.08$ and 0.92, corresponding to electron and hole doping. This suggests that the optimal doping ratio in the Holstein model when $\tau \ll \lambda$ is that HOMOs are 8% filled by holes or LUMOs are 8% filled by electrons. In addition, PF increases with increasing τ monotonically. These all agree with Figure 4e.

3.4. Dependence on the Transfer Integral. As shown in Figure 5a,b, in the strong electron-coupling regime where $\tau \ll \lambda$, the behavior satisfies $\sigma \propto \tau^2$ and $\alpha = -\frac{k_B}{e}\ln\frac{c}{1-c}$ (independent of τ), indicating a hopping-like transport mechanism.[71,73] When τ keeps increasing, both σ and α departure hopping-like behaviors in this intermediate regime. σ keeps increasing with increasing τ but $\sigma \propto \tau^2$ no longer holds. Different from τ irrelevance presented in the strong coupling regime, α begins to decrease with increasing τ. Finally, when $\tau > \lambda$, the transport behavior turns bandlike. On the one hand, conductivity roughly satisfies, $\sigma \propto \tau^{3/2}$, which is considered a typical bandlike behavior.[74] On the other hand, $\alpha - \tau$ dependence becomes similar to $\alpha - \tau$ dependence calculated by the Boltzmann transport equation. Note that the introduction of electron−phonon coupling contributes an additional decrease of α in the bandlike regime in Figure 5b. Considering the wide bandwidth, the decrease of α with increasing τ in the band limit can also be interpreted via Mott's formula[75] because increasing τ leads to a smoother change in $D(E)$ (Supporting Information 6).

$$\alpha = \frac{\pi^2}{3}\frac{k_B}{e}k_B T\frac{d\ln D(E)}{dE}\bigg|_{E=\mu} \tag{31}$$

The power factor PF is also calculated in Figure 5c to measure thermoelectric performance. We find that with other factors fixed, the increase of τ systematically increases PF, enhancing thermoelectric performance.

The crossover of transport behavior from hopping to bandlike is also reflected in the mean free path l_{mfp},[76] shown in Figure 5d. Here

$$l_{\text{mfp}} = v\theta \tag{32}$$

where the mean square velocity is calculated as

$$v = \left[\frac{1}{e^2 n_e}C_1(0)\right]^{1/2} \tag{33}$$

and the coherence time is obtained as

$$\theta = \int_0^{+\infty} dt\left|\frac{\text{Re } C_1(t)}{\text{Re } C_1(0)}\right| \tag{34}$$

In the strong coupling regime, $l_{\text{mfp}}/\Omega \ll 1$ indicates that electrons are totally localized in a single unit cell and the transport process is hopping-like. With the increase of τ, l_{mfp} becomes comparable to Ω, corresponding to the intermediate

regime. Finally, when $l_{mfp}/\Omega \gg 1$, electrons are more delocalized and the bandlike transport behavior appears.

4. CONCLUSIONS

In summary, we developed a numerically nearly exact method for calculating the power factor of organic thermoelectric materials modeled by the electron–phonon (Holstein) model via combining the Kubo formula with the finite-temperature time-dependent density matrix renormalization group (FT-TD-DMRG) in the grand canonical ensemble. We demonstrated the validity and computational feasibility of a broad parameter range. We highlight the advantage of the present method for an intermediate coupling regime, which is difficult for other approximate methods. Our method can bridge the gap between the hopping transport described by Fermi's golden rule and band transport described by the Boltzmann transport equation, providing a unified picture of the organic materials' thermoelectric transport process. We find that (i) the electric conductivity and Seebeck coefficient strongly depend on the doping ratio and present impressive symmetry of about $c = 0.5$ in room temperature and (ii) increasing the transfer integral changes the transport mechanism from hopping to bandlike and enhances the power factor monotonically. By merely changing the exact form of Hamiltonian and current operators, it is straightforward to take other factors into account in our framework, such as the off-diagonal dynamic disorder, Coulombic interaction, static disorder, and so on.

■ ASSOCIATED CONTENT

Ⓢ Supporting Information

The Supporting Information is available free of charge at https://pubs.acs.org/doi/10.1021/acs.jctc.2c00651.

> Derivation of the electron current operator and heat current operator; selection of phonon modes; illustration of the TD-DMRG algorithm's validity; introduction to the Boltzmann transport theory; introduction to the polaron transformation approach; and derivation of expressions of the conductivity and Seebeck coefficient in limiting cases (PDF)

■ AUTHOR INFORMATION

Corresponding Author

Zhigang Shuai − *MOE Key Laboratory of Organic OptoElectronics and Molecular Engineering, Department of Chemistry, Tsinghua University, 100084 Beijing, P. R. China; School of Science and Engineering, The Chinese University of Hong Kong, Shenzhen 518172 Guangdong, P. R. China;* ⓞ orcid.org/0000-0003-3867-2331; Email: zgshuai@tsinghua.edu.cn

Authors

Yufei Ge − *MOE Key Laboratory of Organic OptoElectronics and Molecular Engineering, Department of Chemistry, Tsinghua University, 100084 Beijing, P. R. China;* ⓞ orcid.org/0000-0001-7150-8483

Weitang Li − *MOE Key Laboratory of Organic OptoElectronics and Molecular Engineering, Department of Chemistry, Tsinghua University, 100084 Beijing, P. R. China*

Jiajun Ren − *MOE Key Laboratory of Theoretical and Computational Photochemistry, College of Chemistry, Beijing Normal University, 100875 Beijing, P. R. China;* ⓞ orcid.org/0000-0002-1508-4943

Complete contact information is available at:
https://pubs.acs.org/10.1021/acs.jctc.2c00651

Notes

The authors declare no competing financial interest.

■ REFERENCES

(1) Russ, B.; Glaudell, A.; Urban, J. J.; Chabinyc, M. L.; Segalman, R. A. Organic thermoelectric materials for energy harvesting and temperature control. *Nat. Rev. Mater.* **2016**, *1*, 16050.

(2) Beekman, M.; Morelli, D. T.; Nolas, G. S. Better thermoelectrics through glass-like crystals. *Nat. Mater.* **2015**, *14*, 1182−1185.

(3) He, J.; Tritt, T. M. Advances in thermoelectric materials research: Looking back and moving forward. *Science* **2017**, *357*, No. eaak9997.

(4) Shi, X.; He, J. Thermopower and harvesting heat. *Science* **2021**, *371*, 343−344.

(5) Bubnova, O.; Khan, Z. U.; Wang, H.; Braun, S.; Evans, D. R.; Fabretto, M.; Hojati-Talemi, P.; Dagnelund, D.; Arlin, J.-B.; Geerts, Y. H.; Desbief, S.; Breiby, D. W.; Andreasen, J. W.; Lazzaroni, R.; Chen, W. M.; Zozoulenko, I.; Fahlman, M.; Murphy, P. J.; Berggren, M.; Crispin, X. Semi-metallic polymers. *Nat. Mater.* **2014**, *13*, 190−194.

(6) Wang, Y.; Yang, L.; Shi, X.-L.; Shi, X.; Chen, L.; Dargusch, M. S.; Zou, J.; Chen, Z.-G. Flexible Thermoelectric Materials and Generators: Challenges and Innovations. *Adv. Mater.* **2019**, *31*, No. 1807916.

(7) Liu, J.; van der Zee, B.; Alessandri, R.; Sami, S.; Dong, J.; Nugraha, M. I.; Barker, A. J.; Rousseva, S.; Qiu, L.; Qiu, X.; Klasen, N.; Chiechi, R. C.; Baran, D.; Caironi, M.; Anthopoulos, T. D.; Portale, G.; Havenith, R. W. A.; Marrink, S. J.; Hummelen, J. C.; Koster, L. J. A. N-type organic thermoelectrics: demonstration of ZT 0.3. *Nat. Commun.* **2020**, *11*, No. 5694.

(8) Sun, Y.; Qiu, L.; Tang, L.; Geng, H.; Wang, H.; Zhang, F.; Huang, D.; Xu, W.; Yue, P.; Guan, Y.-S.; Jiao, F.; Sun, Y.; Tang, D.; Di, C.-A.; Yi, Y.; Zhu, D. Flexible n-Type High-Performance Thermoelectric Thin Films of Poly(nickel-ethylenetetrathiolate) Prepared by an Electrochemical Method. *Adv. Mater.* **2016**, *28*, 3351−3358.

(9) Kim, G.-H.; Shao, L.; Zhang, K.; Pipe, K. P. Engineered doping of organic semiconductors for enhanced thermoelectric efficiency. *Nat. Mater.* **2013**, *12*, 719−723.

(10) Rowe, D. M. *Thermoelectrics Handbook: Macro to Nano*; CRC/Taylor & Francis: Boca Raton, FL, 2006.

(11) Kittel, C. *Introduction to Solid State Physics*, 8th ed.; Wiley: Hoboken, NJ, 2005.

(12) Wang, D.; Shi, W.; Chen, J.; Xi, J.; Shuai, Z. Modeling thermoelectric transport in organic materials. *Phys. Chem. Chem. Phys.* **2012**, *14*, 16505−16520.

(13) Gao, X.; Uehara, K.; Klug, D. D.; Patchkovskii, S.; Tse, J. S.; Tritt, T. M. Theoretical studies on the thermopower of semiconductors and low-band-gap crystalline polymers. *Phys. Rev. B* **2005**, *72*, No. 125202.

(14) Yang, J.; Li, H.; Wu, T.; Zhang, W.; Chen, L.; Yang, J. Evaluation of Half-Heusler Compounds as Thermoelectric Materials Based on the Calculated Electrical Transport Properties. *Adv. Funct. Mater.* **2008**, *18*, 2880−2888.

(15) Shi, W.; Zhao, T.; Xi, J.; Wang, D.; Shuai, Z. Unravelling Doping Effects on PEDOT at the Molecular Level: From Geometry to Thermoelectric Transport Properties. *J. Am. Chem. Soc.* **2015**, *137*, 12929−12938.

(16) Shi, W.; Wang, D.; Shuai, Z. High-Performance Organic Thermoelectric Materials: Theoretical Insights and Computational Design. *Adv. Electron. Mater.* **2019**, *5*, No. 1800882.

(17) Kang, S. D.; Jeffrey Snyder, G. Charge-transport model for conducting polymers. *Nat. Mater.* **2017**, *16*, 252−257.

(18) Gregory, S. A.; Hanus, R.; Atassi, A.; Rinehart, J. M.; Wooding, J. P.; Menon, A. K.; Losego, M. D.; Snyder, G. J.; Yee, S. K. Quantifying charge carrier localization in chemically doped semiconducting polymers. *Nat. Mater.* **2021**, *20*, 1414−1421.

(19) Fratini, S.; Nikolka, M.; Salleo, A.; Schweicher, G.; Sirringhaus, H. Charge transport in high-mobility conjugated polymers and molecular semiconductors. *Nat. Mater.* **2020**, *19*, 491−502.

(20) Schweicher, G.; D'Avino, G.; Ruggiero, M. T.; Harkin, D. J.; Broch, K.; Venkateshvaran, D.; Liu, G.; Richard, A.; Ruzié, C.; Armstrong, J.; Kennedy, A. R.; Shankland, K.; Takimiya, K.; Geerts, Y. H.; Zeitler, J. A.; Fratini, S.; Sirringhaus, H. Chasing the "Killer" Phonon Mode for the Rational Design of Low-Disorder, High-Mobility Molecular Semiconductors. *Adv. Mater.* **2019**, *31*, No. 1902407.

(21) Giannini, S.; Carof, A.; Ellis, M.; Yang, H.; Ziogos, O. G.; Ghosh, S.; Blumberger, J. Quantum localization and delocalization of charge carriers in organic semiconducting crystals. *Nat. Commun.* **2019**, *10*, No. 3843.

(22) Tessler, N.; Preezant, Y.; Rappaport, N.; Roichman, Y. Charge Transport in Disordered Organic Materials and Its Relevance to Thin-Film Devices: A Tutorial Review. *Adv. Mater.* **2009**, *21*, 2741−2761.

(23) Coropceanu, V.; Cornil, J.; Da Silva Filho, D. A.; Olivier, Y.; Silbey, R.; Brédas, J.-L. Charge transport in organic semiconductors. *Chem. Rev.* **2007**, *107*, 926−952.

(24) Lu, N.; Li, L.; Liu, M. Universal carrier thermoelectric-transport model based on percolation theory in organic semiconductors. *Phys. Rev. B* **2015**, *91*, No. 195205.

(25) Lu, N.; Li, L.; Liu, M. A review of carrier thermoelectric-transport theory in organic semiconductors. *Phys. Chem. Chem. Phys.* **2016**, *18*, 19503−19525.

(26) Ihnatsenka, S.; Crispin, X.; Zozoulenko, I. V. Understanding hopping transport and thermoelectric properties of conducting polymers. *Phys. Rev. B* **2015**, *92*, 35201.

(27) Crispin, X.; Kalinin, S. V. Semiconducting polymers: Probing the solid-liquid interface. *Nat. Mater.* **2017**, *16*, 704−705.

(28) Oberhofer, H.; Reuter, K.; Blumberger, J. Charge Transport in Molecular Materials: An Assessment of Computational Methods. *Chem. Rev.* **2017**, *117*, 10319−10357.

(29) Emin, D. *Polarons*; Cambridge University Press: Cambridge, UK, 2013.

(30) Fetherolf, J. H.; Golež, D.; Berkelbach, T. C. A Unification of the Holstein Polaron and Dynamic Disorder Pictures of Charge Transport in Organic Crystals. *Phys. Rev. X* **2020**, *10*, 21062.

(31) Hutsch, S.; Panhans, M.; Ortmann, F. Time-consistent hopping transport with vibration-mode-resolved electron-phonon couplings. *Phys. Rev. B* **2021**, *104*, 54306.

(32) Nematiaram, T.; Troisi, A. Modeling charge transport in high-mobility molecular semiconductors: Balancing electronic structure and quantum dynamics methods with the help of experiments. *J. Chem. Phys.* **2020**, *152*, No. 190902.

(33) Hannewald, K.; Stojanović, V. M.; Schellekens, J. M. T.; Bobbert, P. A.; Kresse, G.; Hafner, J. Theory of polaron bandwidth narrowing in organic molecular crystals. *Phys. Rev. B* **2004**, *69*, 75211.

(34) Hannewald, K.; Bobbert, P. A. Anisotropy effects in phonon-assisted charge-carrier transport in organic molecular crystals. *Phys. Rev. B* **2004**, *69*, 75212.

(35) Ortmann, F.; Bechstedt, F.; Hannewald, K. Theory of charge transport in organic crystals: Beyond Holstein's small-polaron model. *Phys. Rev. B* **2009**, *79*, No. 235206.

(36) Wang, Y.-C.; Zhao, Y. Variational polaron transformation approach toward the calculation of thermopower in organic crystals. *Phys. Rev. B* **2020**, *101*, No. 075205.

(37) Wang, Y.; Zhou, J.; Yang, R. Thermoelectric Properties of Molecular Nanowires. *J. Phys. Chem. C* **2011**, *115*, 24418−24428.

(38) Xu, D.; Cao, J. Non-canonical distribution and non-equilibrium transport beyond weak system-bath coupling regime: A polaron transformation approach. *Front. Phys.* **2016**, *11*, No. 110308.

(39) Xie, W.; Holub, D.; Kubař, T.; Elstner, M. Performance of Mixed Quantum-Classical Approaches on Modeling the Crossover from Hopping to Bandlike Charge Transport in Organic Semiconductors. *J. Chem. Theory. Comput.* **2020**, *16*, 2071−2084.

(40) Nijjar, P.; Jankowska, J.; Prezhdo, O. V. Ehrenfest and classical path dynamics with decoherence and detailed balance. *J. Chem. Phys.* **2019**, *150*, No. 204124.

(41) Birch, S. W.; Pipe, K. P. Effects of dynamic disorder on thermoelectric transport in soft materials. *J. Appl. Phys.* **2022**, *131*, No. 135104.

(42) Troisi, A.; Orlandi, G. Charge-transport regime of crystalline organic semiconductors: diffusion limited by thermal off-diagonal electronic disorder. *Phys. Rev. Lett.* **2006**, *96*, 86601.

(43) Troisi, A. Charge transport in high mobility molecular semiconductors: classical models and new theories. *Chem. Soc. Rev.* **2011**, *40*, 2347−2358.

(44) Fratini, S.; Ciuchi, S.; Mayou, D.; Laissardière, G. T. de.; Troisi, A. A map of high-mobility molecular semiconductors. *Nat. Mater.* **2017**, *16*, 998−1002.

(45) Troisi, A.; Cheung, D. L.; Andrienko, D. Charge transport in semiconductors with multiscale conformational dynamics. *Phys. Rev. Lett.* **2009**, *102*, No. 116602.

(46) Ren, J.; Li, W.; Jiang, T.; Wang, Y.; Shuai, Z. Time-dependent density matrix renormalization group method for quantum dynamics in complex systems. *WIREs Comput. Mol. Sci.* **2022**, *3145*, 293.

(47) White, S. R. Density matrix formulation for quantum renormalization groups. *Phys. Rev. Lett.* **1992**, *69*, 2863−2866.

(48) Schollwöck, U. The density-matrix renormalization group in the age of matrix product states. *Ann. Phys.* **2011**, *326*, 96−192.

(49) Paeckel, S.; Köhler, T.; Swoboda, A.; Manmana, S. R.; Schollwöck, U.; Hubig, C. Time-evolution methods for matrix-product states. *Ann. Phys.* **2019**, *411*, No. 167998.

(50) Verstraete, F.; Murg, V.; Cirac, J. I. Matrix product states, projected entangled pair states, and variational renormalization group methods for quantum spin systems. *Adv. Phys.* **2008**, *57*, 143−224.

(51) Liao, H. J.; Xie, Z. Y.; Chen, J.; Liu, Z. Y.; Xie, H. D.; Huang, R. Z.; Normand, B.; Xiang, T. Gapless Spin-Liquid Ground State in the S=1/2 Kagome Antiferromagnet. *Phys. Rev. Lett.* **2017**, *118*, No. 137202.

(52) Chan, G. K.-L.; Keselman, A.; Nakatani, N.; Li, Z.; White, S. R. Matrix product operators, matrix product states, and ab initio density matrix renormalization group algorithms. *J. Chem. Phys.* **2016**, *145*, 14102.

(53) Baiardi, A.; Reiher, M. Large-Scale Quantum Dynamics with Matrix Product States. *J. Chem. Theory. Comput.* **2019**, *15*, 3481−3498.

(54) Ren, J.; Shuai, Z.; Kin-Lic Chan, G. Time-Dependent Density Matrix Renormalization Group Algorithms for Nearly Exact Absorption and Fluorescence Spectra of Molecular Aggregates at Both Zero and Finite Temperature. *J. Chem. Theory. Comput.* **2018**, *14*, 5027−5039.

(55) Li, W.; Ren, J.; Shuai, Z. Numerical assessment for accuracy and GPU acceleration of TD-DMRG time evolution schemes. *J. Chem. Phys.* **2020**, *152*, 24127.

(56) Ren, J.; Li, W.; Jiang, T.; Shuai, Z. A general automatic method for optimal construction of matrix product operators using bipartite graph theory. *J. Chem. Phys.* **2020**, *153*, 84118.

(57) Li, W.; Ren, J.; Shuai, Z. Finite-Temperature TD-DMRG for the Carrier Mobility of Organic Semiconductors. *J. Phys. Chem. Lett.* **2020**, *11*, 4930−4936.

(58) Li, W.; Ren, J.; Shuai, Z. A general charge transport picture for organic semiconductors with nonlocal electron-phonon couplings. *Nat. Commun.* **2021**, *12*, No. 4260.

(59) Holstein, T. Studies of Polaron Motion: Part II The "Small" Polaron. *Ann. Phys.* **1959**, *281*, 725−773.

(60) Mahan, G. D.*Many-Particle Physics*, 3rd ed.; Kluwer Academic/Plenum Publishers: New York, 2000.

(61) Li, W.; Ren, J.; Yang, H.; Shuai, Z. On the fly swapping algorithm for ordering of degrees of freedom in density matrix renormalization group. *J. Phys. Condens. Matter.* **2022**, *34*, No. 254003.

(62) Barcza, G.; Legeza, Ö.; Marti, K. H.; Reiher, M. Quantum-information analysis of electronic states of different molecular structures. *Phys. Rev. A* **2011**, *83*, 298.

(63) Rissler, J.; Noack, R. M.; White, S. R. Measuring orbital interaction using quantum information theory. *Chem. Phys.* **2006**, *323*, 519−531.

(64) Moritz, G.; Hess, B. A.; Reiher, M. Convergence behavior of the density-matrix renormalization group algorithm for optimized orbital orderings. *J. Chem. Phys.* **2005**, *122*, 24107.

(65) White, S. R.; Feiguin, A. E. Real-time evolution using the density matrix renormalization group. *Phys. Rev. Lett.* **2004**, *93*, 76401.

(66) Vidal, G. Efficient simulation of one-dimensional quantum many-body systems. *Phys. Rev. Lett.* **2004**, *93*, 40502.

(67) Haegeman, J.; Lubich, C.; Oseledets, I.; Vandereycken, B.; Verstraete, F. Unifying time evolution and optimization with matrix product states. *Phys. Rev. B* **2016**, *94*, No. 165116.

(68) Verstraete, F.; García-Ripoll, J. J.; Cirac, J. I. Matrix product density operators: simulation of finite-temperature and dissipative systems. *Phys. Rev. Lett.* **2004**, *93*, No. 207204.

(69) Lange, F.; Ejima, S.; Fehske, H. Strongly repulsive anyons in one dimension. *Phys. Rev. A* **2017**, *95*, 63621.

(70) Fritzsche, H. A general expression for the thermoelectric power. *Solid State Commun.* **1971**, *9*, 1813−1815.

(71) Schotte, K. D. The thermoelectric properties of the small polaron. *Z. Physik* **1966**, *196*, 393−414.

(72) Emin, D. Enhanced Seebeck coefficient from carrier-induced vibrational softening. *Phys. Rev. B* **1999**, *59*, 6205−6210.

(73) Nan, G.; Yang, X.; Wang, L.; Shuai, Z.; Zhao, Y. Nuclear tunneling effects of charge transport in rubrene, tetracene, and pentacene. *Phys. Rev. B* **2009**, *79*, No. 115203.

(74) Glarum, S. H. Electron mobilities in organic semiconductors. *J. Phys. Chem. Solids* **1963**, *24*, 1577−1583.

(75) Cutler, M.; Mott, N. F. Observation of Anderson Localization in an Electron Gas. *Phys. Rev.* **1969**, *181*, 1336−1340.

(76) Prodanović, N.; Vukmirović, N. Charge carrier mobility in systems with local electron-phonon interaction. *Phys. Rev. B* **2019**, *99*, No. 104304.

▣ Recommended by ACS